Guo et al. *Microsystems & Nanoengineering* (2026)12:218
https://doi.org/10.1038/s41378-026-01349-3

Microsystems & Nanoengineering
www.nature.com/micronano

ARTICLE Open Access

Intelligent label-free droplet microfluidic sorting system for single-cell encapsulation and morphology-guided screening

Kefan Guo[1,2], Qingqing Liu[1], Huiling Yuan[3,4], Yuanyuan Zhang[3,4], Zhixian Zhu[1], Shu Zhu[1], Lin Jiang[1], Qinhong Wang[3,4]✉ and Nan Xiang[1]✉

Abstract

The label-free extraction of cellular morphological data from within droplet microenvironments, and its subsequent translation into reliable, high-precision sorting, continues to pose a central challenge in the field of droplet microfluidics. Here, we develop an intelligent label-free droplet sorting (ILFDS) system by integrating droplet microfluidics, real-time image recognition, and dielectrophoresis (DEP) sorting. The developed system operates at low voltages (250–350 V) by using the innovative liquid-metal electrodes, which enable real-time sorting while minimizing droplet deformation and preserving cell integrity. In experiments on sorting single-target encapsulated droplets, the ILFDS system achieves detection accuracies of >98% and sorting efficiencies of >85% for particles, *Haematococcus pluvialis*, and *Scenedesmus quadricauda*, with the proportion of single-target droplets increasing by approximately 3.15-fold, 11.37-fold, and 4.59-fold, respectively, after sorting. Furthermore, the ILFDS system demonstrates high-precision sorting of targets from mixed samples based on morphological features, achieving detection accuracies of above 90% and sorting efficiencies of over 89% for mixed *Haematococcus pluvialis* and *Euglena gracilis* samples. These results highlight the system's robustness in handling heterogeneous samples and its capability to overcome key limitations associated with conventional droplet encapsulation and detection. By enabling scalable, high-throughput, and label-free sorting based on image recognition, our ILFDS system offers a versatile platform for a wide range of droplet-based analytical and screening applications.

Introduction

Single-cell analysis has emerged as the cornerstone of modern biological research, offering a powerful means to probe into the cellular heterogeneity and to uncover the mechanisms driving both physiological function and disease pathology[1–3]. This capability is very important for understanding disease progression, identifying new therapeutic targets, and advancing personalized medicine[4–7]. To achieve these objectives, the development of analytical techniques capable of providing both precise single-cell isolation and compatibility with high-throughput molecular profiling is essential[8–10].

Among the developed techniques, droplet microfluidics has shown strong potential as a practical approach for isolating and analyzing single cells within discrete and controllable microenvironments[11–13]. The physical and chemical isolation afforded by droplets minimizes cross-contamination, reduces reagent consumption, and enables massively parallel biochemical reactions[14–16]. Integrated modules for droplet generation, reagent delivery, incubation, and on-chip detection have allowed droplet microfluidics to transform applications, including single-cell genomics, directed evolution, and high-throughput microbial or algal

Correspondence: Qinhong Wang (wang_qh@tib.cas.cn) or Nan Xiang (nan.xiang@seu.edu.cn)
[1]School of Mechanical Engineering, and Jiangsu Key Laboratory for Design and Manufacture of Micro-Nano Biomedical Instruments, Southeast University, Nanjing, China
[2]Department of Mechanical Engineering, The University of Hong Kong, Pokfulam, Hong Kong, China
Full list of author information is available at the end of the article
These authors contributed equally: Kefan Guo, Qingqing Liu

© The Author(s) 2026
Open Access This article is licensed under a Creative Commons Attribution-NonCommercial-NoDerivatives 4.0 International License, which permits any non-commercial use, sharing, distribution and reproduction in any medium or format, as long as you give appropriate credit to the original author(s) and the source, provide a link to the Creative Commons licence, and indicate if you modified the licensed material. You do not have permission under this licence to share adapted material derived from this article or parts of it. The images or other third party material in this article are included in the article's Creative Commons licence, unless indicated otherwise in a credit line to the material. If material is not included in the article's Creative Commons licence and your intended use is not permitted by statutory regulation or exceeds the permitted use, you will need to obtain permission directly from the copyright holder. To view a copy of this licence, visit http://creativecommons.org/licenses/by-nc-nd/4.0/.

screening[17–19]. However, the passive encapsulation process is inherently governed by Poisson statistics, leading to a substantial fraction of empty or multi-cell droplets and reducing the efficiency of single-cell workflows.

Fluorescence-activated droplet sorting (FADS) has expanded the utility of droplet microfluidics by enabling high-throughput detection and sorting based on fluorescent biochemical signals[20]. Compared with conventional fluorescence-activated cell sorting (FACS), the droplet environment better preserves cell viability and retains secreted molecules, supporting ultrahigh-throughput screening of enzymes, antibodies, and metabolites[21–24]. However, fluorescence readouts intrinsically limit the analytical resolution of FADS[25]. Because the measured signal represents only the integrated fluorescence intensity of each droplet, FADS cannot determine whether a droplet contains zero, one, or multiple cells, resulting in misclassification under Poisson encapsulation[26,27]. Fluorescent labeling is also constrained by low biomarker expression and dye instability, and introduces potential perturbation to cell physiology[28]. Moreover, fluorescence provides low-dimensional information and cannot capture richer morphological or biophysical features[5]. These constraints highlight the need for label-free detection methods that can characterize cells in droplets at a higher information depth.

To address this challenge, there is growing interest in developing label-free detection techniques based on imaging signals for droplet sorting, which couple bright-field imaging with machine-vision analysis and active microfluidic sorting. Image-based droplet detection has been used to distinguish single-cell droplets from multi-cell droplets and alleviate Poisson-loading limitations[21,29], while deep-learning classifiers further improve the detection accuracy[30]. YOLO-based detectors have enabled real-time recognition of multiple encapsulated objects within individual droplets, and impedance-activated sorting platforms offer complementary label-free quantification of cell number in droplets[31]. Although these developments substantially expand the analytical depth of droplet sorting, most existing systems remain restricted to simple applications on detecting cell number in droplets, exhibit limited robustness when processing heterogeneous biological samples such as mixed algae or multi-species microbial suspensions[32,33], and frequently rely on relatively high actuation voltages that introduce considerable droplet deformation and potential cell stress[34,35]. Representative image-based droplet sorting studies have demonstrated automated single-cell enrichment and real-time sorting verification, deep-learning-guided classification and sorting of droplets containing single cells, multiple objects, or 3D cell cultures, as well as gray-level-guided discrimination of empty-, single-, and multi-cell droplets[30,36,37]. Nevertheless, these systems remain primarily focused on droplet occupancy or object-count-based classification, with limited emphasis on morphology-based discrimination of heterogeneous biological targets under continuous-flow conditions. These limitations underscore the need for an intelligent droplet sorting system that extends beyond droplet occupancy detection toward morphology-based, label-free discrimination, while maintaining low-voltage and deformation-minimized operation.

In this study, we developed an intelligent label-free droplet sorting (ILFDS) system that integrates droplet microfluidics, real-time image recognition, and dielectrophoretic (DEP) actuation to overcome the inherent randomness of encapsulation and enable morphology-based, label-free sorting. Distinct from previous image-based droplet sorting strategies that primarily focus on droplet occupancy or object-count-based classification, the present system is designed for the selective discrimination of heterogeneous micro-targets according to morphological features under continuous-flow conditions. In addition, a qualitative comparison with representative commercially available image-based cell analysis/sorting platforms is provided in Table S1 to further clarify the positioning of the present ILFDS system. By combining YOLO-enabled image detection with robot operating system (ROS)-based hardware–software coordination, the ILFDS system achieves efficient data acquisition, real-time decision making, and synchronized downstream actuation. In addition, liquid-metal electrodes enable real-time sorting at low voltages (250–350 V), minimizing droplet deformation and preserving droplet integrity. Our experiments on sorting single-target encapsulated droplets demonstrate detection accuracies above 98% and sorting efficiencies exceeding 85% for 30 μm polystyrene particles, *Haematococcus pluvialis*, and *Scenedesmus quadricauda*. Additionally, experiments with mixed algae solutions confirm that the ILFDS system effectively sorts targets from complex samples based on morphology differences, achieving detection accuracies of over 90%. These results establish the ILFDS system as a promising platform for label-free single-cell analysis and morphology-guided screening applications.

Materials and methods

Device fabrication and assembly

The fabrication of our microfluidic device was achieved using soft lithography and oxygen plasma bonding techniques. Specifically, a silicon wafer was first coated with a layer of 50 μm thick SU-8 2025 negative photoresist (MicroChem) using spin-coating. Followed by the soft baking step, UV exposure was performed for 15 s under a patterned photomask in an exposure machine (MJB4, SUSS MicroTec). The wafer was then developed in SU-8 developer (MicroChem) for 3–5 min to dissolve the unexposed

photoresist for creating the master mold. Subsequently, a 10:1 ratio mixture of polydimethylsiloxane (PDMS, Sylgard 184, Dow Corning) was poured onto the master mold and cured at 65 °C for two hours. After demolding and cutting, the PDMS was bonded to a glass slide using an oxygen plasma cleaner (PDC-002, Harrick Plasma). The final step involved injecting liquid metal into the reserved electrode structure in the PDMS layer to fabricate the liquid-metal electrodes. The liquid metal used for the electrodes had a Ga/In weight ratio of 75/25.

Experimental setup and data analysis

To consistently generate droplets encapsulated with targets, high-precision syringe pumps (Pump 33DDS, Harvard Apparatus) were used for sample and oil injection. The chip inlet was seamlessly interfaced with the syringe via Teflon tubing, while the chip outlets were interfaced with collection and waste tubes, respectively. To dynamically capture targets within the droplets, we used a back-illuminated CMOS camera (Prime BSI Express, Teledyne Photometrics). The microfluidic chip was securely positioned on the platform of an upright microscope (ECLIPSE 80i, Nikon), which facilitated the real-time visualization of the observation region through the CMOS camera.

To enhance the efficiency of droplet detection, we used a vision tower graphic workstation (Precision 3660, Dell) equipped with NVIDIA GeForce RTX3090 and CPU i9 12900k, and configured the workstation with a dual-operating system environment. Contrasted with the singular system setup, the dual-operating system environment increases the computational efficiency of machine vision and neural network algorithms. Additionally, the node connectivity approach within the Ubuntu framework enables the rapid integration and linkage of multiple communication devices, paving the way for real-time processing. During experimental runs, we employed the RVIZ software within the Ubuntu 20.04 environment to append image nodes and capture data from both the CMOS camera's ROS node "BSI PVCAM" and the neural network's image detection ROS node "Publisher Output". The data analysis segment leveraged a deep-learning environment, including Python 3.8, CUDA 11.3, and Pytorch 1.12.0.

Electromagnetic isolation was accomplished by using a signal isolator (ADUM3160, AMSAMOTION), which was connected to the droplet sorting controller to receive output signals from the neural network. To ensure precise droplet sorting within the system, we employed a voltage amplifier (ATA-7100, Aigtek). The amplifier was interconnected with the droplet sorting controller, an oscilloscope (UTD2102CEX+, NI-T), and the liquid-metal electrodes within the microfluidic chip. Figure S1 illustrates the detailed physical diagram of the ILFDS system.

Sample preparation

To evaluate the detection and sorting capabilities of the ILFDS system, we used fluorescent polystyrene beads (diameter: 30 μm, 1% w/v, Biotyscience) as surrogate biological particles. These beads were diluted in phosphate-buffered saline (PBS, Sigma-Aldrich) to a concentration of 1×10^6 counts/mL.

To further validate the system's sorting efficacy for different algae species, we used *Scenedesmus quadricauda* at a concentration of 1×10^6 counts/mL, *Haematococcus pluvialis* at a concentration of 1×10^4 counts/mL, and *Euglena gracilis* at a concentration of 1×10^6 counts/mL. Prior to droplet encapsulation, the algal cultures were homogenized under sterile conditions and transferred to culture flasks. The cultures were then incubated under a 12-h light/12-h dark cycle with an illumination intensity of 1000–2000 lux at 25 °C for 2–3 days in a sterile incubator. Both algal species were procured from the Freshwater Algae Culture Collection at the Institute of Hydrobiology, Chinese Academy of Sciences. During the droplet generation process, the oil phase was electronic fluorinated liquid HFE7500 (DPFO2210017, Drop-Surf) containing 2% surfactant, and the aqueous phase was phosphate-buffered saline (PBS).

Results and discussion

Design of the ILFDS system

To achieve label-free detection and real-time sorting of target droplets, we developed an ILFDS system integrating droplet microfluidics, YOLO-D-based image recognition, and dielectrophoretic actuation. As illustrated in Fig. 1a, the system consists of five functional regions for droplet generation, spacing, detection, sorting, and collection. In the droplet generation region, various micro-targets are encapsulated using a flow-focusing structure by adjusting the flow rates of the oil and aqueous phases. As shown in Fig. 1b, droplets containing different numbers and types of micro-targets are generated in this region, and the number of encapsulated targets follows Poisson statistics. In the spacing region, additional fluorinated oil is introduced through branch channels to increase the distance between adjacent droplets, thereby reducing droplet-droplet interference and improving the accuracy of downstream detection and sorting. The schematic design and fabrication process of the microfluidic chip are shown in Fig. S2.

As droplets pass through the detection region, a complementary metal-oxide-semiconductor (CMOS) camera captures real-time images. To enable efficient data processing and transmission, ROS is adopted as the communication framework, as shown in Fig. 1c. The PVCAM library of the camera is configured as an independent ROS node for continuous image transmission, while the YOLO-D detection node subscribes to the camera image

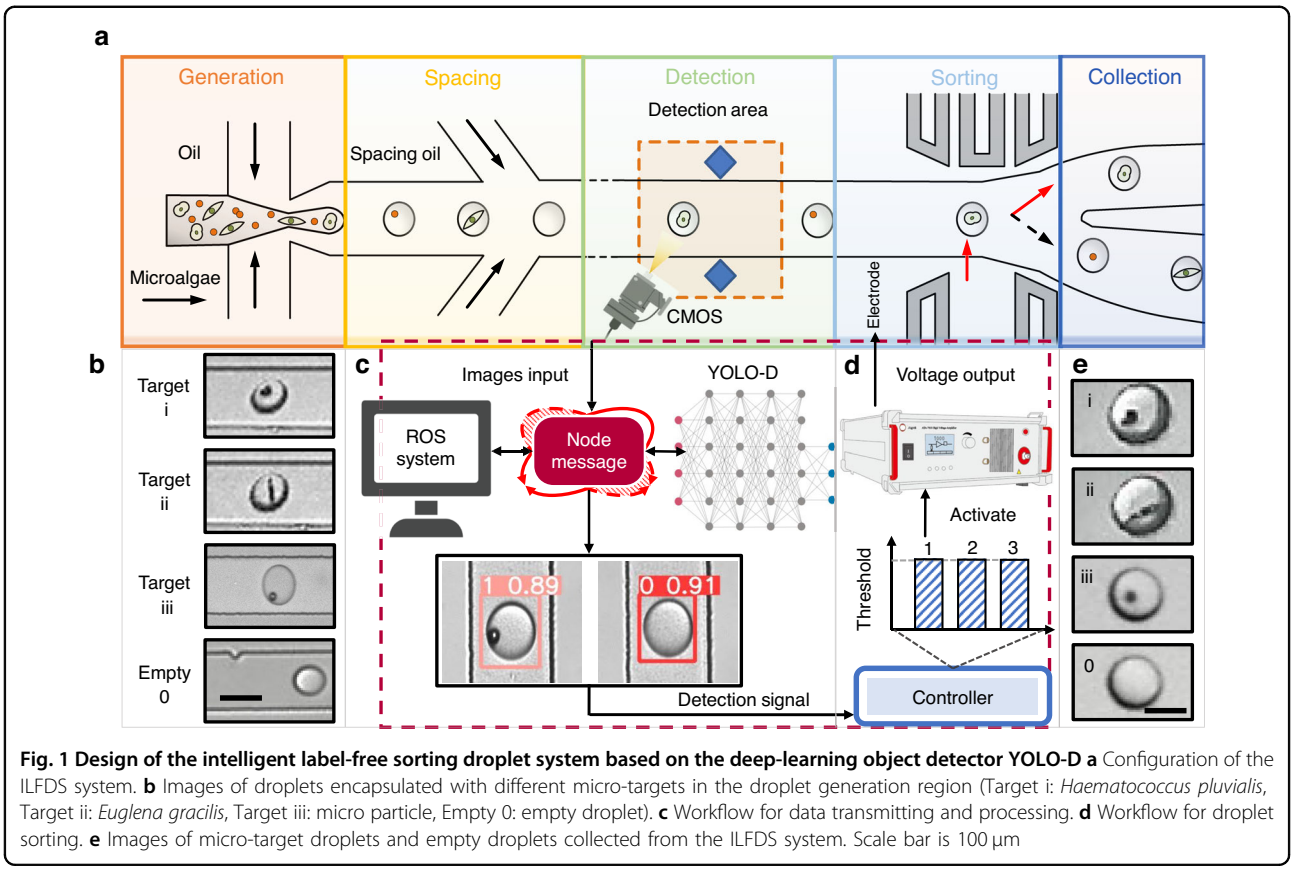

Fig. 1 Design of the intelligent label-free sorting droplet system based on the deep-learning object detector YOLO-D a Configuration of the ILFDS system. **b** Images of droplets encapsulated with different micro-targets in the droplet generation region (Target i: *Haematococcus pluvialis*, Target ii: *Euglena gracilis*, Target iii: micro particle, Empty 0: empty droplet). **c** Workflow for data transmitting and processing. **d** Workflow for droplet sorting. **e** Images of micro-target droplets and empty droplets collected from the ILFDS system. Scale bar is 100 μm

stream and performs real-time target recognition. After model calibration, the system identifies the position and class information of droplets and converts the recognition results into serial signals for downstream sorting control. Image acquisition, neural network detection, and signal transmission are executed in parallel through the ROS-based architecture, enabling continuous droplet analysis and efficient temporal coordination between detection and downstream sorting under continuous-flow conditions. The processed image data are further published to the "Publisher Output" node and displayed in the graphical observation interface. Fig. S3 presents the image acquisition and transmission process together with the ROS node configuration. This modular architecture enables rapid image communication and flexible integration of the detection and sorting modules.

In the sorting region, as depicted in Fig. 1d, the image recognition signal is transmitted to the droplet sorting controller through a USB-TTL serial port with a baud rate of 115,200. The controller outputs a 10 kHz square-wave signal to drive the voltage amplifier, which applies an actuation voltage to the liquid-metal electrodes and generates a non-uniform AC electric field in the sorting region. Under this field, the dielectric contrast between the aqueous droplets and the surrounding fluorinated oil gives rise to positive dielectrophoresis, driving target droplets toward the high-field region and thereby enabling controlled lateral deflection into the collection channel. The DEP response is therefore governed by the electric-field gradient established by the electrode configuration rather than by the applied voltage alone, and the non-uniform sorting field is formed by the asymmetric liquid-metal electrode arrangement at the junction. In the collection region shown in Fig. 1e, target droplets are deflected into the upper collection channel under DEP actuation, while non-target droplets continue along their original trajectories into the waste outlet, completing the label-free sorting process.

The use of liquid-metal electrodes facilitates DEP actuation at relatively moderate voltages by enabling close integration of the electrode structures with the microchannel, thereby enhancing the local electric-field gradient near the droplet path. Compared with conventional electrode implementations such as low-melting-point solder or salt-water electrodes, this configuration provides reduced effective electrode spacing and a more uniform electric-field distribution. This design principle is consistent with our previous study on optimized liquid-metal electrodes for low-voltage droplet sorting[38], in which improved electrode geometry and the high

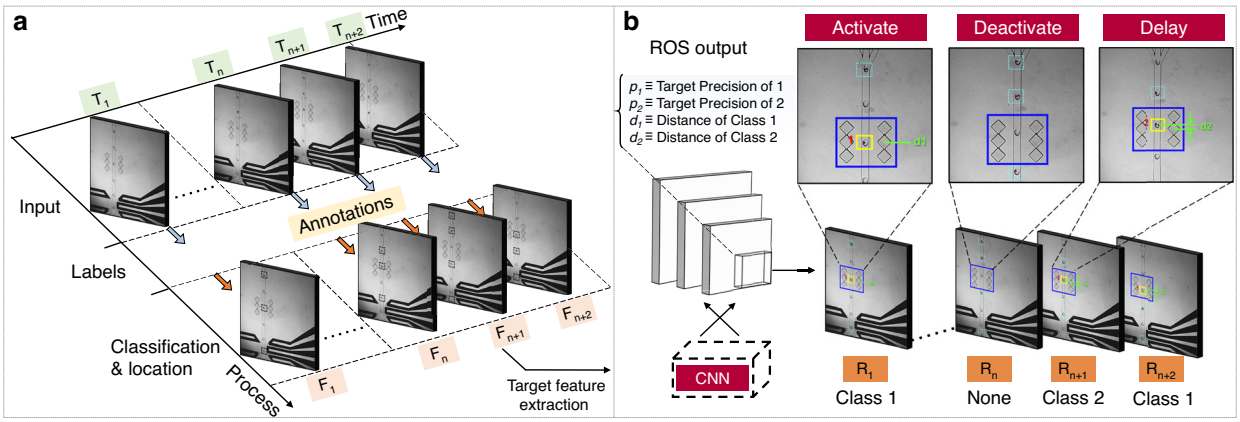

Fig. 2 Training and data analysis process of the ILFDS system a Image training process of the network. The target droplets in each image were annotated, and the classes and positional coordinates of the target droplets within each image were used as the objective features for neural network learning. **b** Signal output patterns of different detection states in the ILFDS system and ROS output results of target detection efficiency, as well as target distance

electrical conductivity of liquid metal were shown to reduce the driving voltage required for effective droplet deflection. In this context, the operating voltage of 250–350 V used in the present ILFDS system falls within the relatively low range of reported DEP droplet sorting platforms, while still providing stable and reliable droplet deflection.

DEP actuation in the present system is performed in a fluorinated oil-aqueous two-phase system with relatively low background conductivity, which supports a stable electric-field distribution and suppresses Joule heating during operation. Under such conditions, reliable droplet deflection can be achieved without significant thermal disturbance. For higher-conductivity media, such as typical cell culture environments, the DEP response and thermal effects may vary, and corresponding adjustment of operating parameters would be required.

Training and optimization of a neural network

YOLO-D is selected for its exceptional performance in high-speed droplet detection and sorting, which is crucial for our system to operate at a high throughput. To achieve high accuracy in model training, we construct a comprehensive image dataset comprising over 1000 time-series droplet images collected under varying lighting, positions, and angles (Fig. 2a). The dataset is annotated with bounding boxes and class labels, and then split into training, validation, and test sets in a ratio of 7:2:1. Data augmentation techniques such as random rotations, scaling, and brightness adjustments are applied. Furthermore, to prevent overfitting, a 5-fold cross-validation strategy is implemented during training. The dataset was collected from experimental runs under varying droplet conditions, including differences in droplet spacing, target morphology, and background characteristics within the microchannel. Together with the applied data augmentation strategies, these variations provide sufficient diversity for training under practical operating conditions of the ILFDS system.

To achieve the high-precision droplet detection and real-time sorting, our ILFDS system processes droplet images through the YOLO-D neural network, which subdivides images into grids for deep feature extraction and target localization, as shown in Fig. 2b. The system accurately predicts droplet categories and bounding boxes for each grid, enabling precise identification of target droplets and outputting their parameters. During real-time detection, the prediction accuracies for target and non-target droplets are evaluated. Once a defined accuracy threshold is met, the system triggers a detection signal. Detection is focused on regions of interest (ROI) within diamond-shaped areas of the images. Representative examples of the raw camera frame, the detection region used for real-time detection and downstream triggering, and the enlarged native-resolution input view are provided in Fig. S4. Using template matching and non-maximum suppression (NMS), the system ensures that optimal bounding boxes are selected for each target droplet.

To enable accurate droplet sorting, the ILFDS system first calculates the required delay based on droplet velocity, camera latency, algorithm response time, and manual calibration. It then generates control signals according to the droplet's position relative to the detection center. When a droplet 1 is centered ($d1 = 0$), the network identifies the droplet and a signal is sent to the electrodes after a preset delay to activate sorting based on the droplet's speed. If the droplet is outside the detection area, no

signal is sent to avoid interference. When droplet 2 is off-center ($d2 \neq 0$), our ILFDS system calculates the necessary delay based on the droplet's speed and position and then sends the signal to ensure precise sorting.

To enhance the detection capabilities for fast-moving droplets, the YOLO-D in our ILFDS system is built based on YOLOv5, a computationally efficient CNN model that is crucial for real-time applications requiring both speed and accuracy[39,40]. YOLOv5 offers several model variants (*n*, *s*, *m*, *l*, and *x*) with different network depths and widths[41,42]. We conduct comparative analyses of these models using the 30 μm particle dataset with consistent parameters and hardware configurations. The input image size is standardized to 1024×1024 pixels to capture essential details and optimize detection accuracy. As shown in Fig. S5A, over 90% precision is achieved by the 90th epoch in models *x*, *l*, *m*, and *s*, while the precision maintains stable thereafter. But the model *n* achieves a lower precision of 92.36% compared with others and shows a small improvement in later epochs. In addition, *x*, *l*, and *m* models reduce loss significantly by the 90th epoch, while *s* and *n* models show slower reduction rates.

Considering a 95% precision threshold as indicative of high accuracy, the time required for each model to reach this level is compared, and the results are illustrated in Fig. S5B. The training time increases from 6.08 min for the model *n* to 36.75 min for the model *x* with the increase of model complexity. Despite the potential for a higher precision using more complex models, our results demonstrated that simple structures like YOLOv5s offer a better balance between detection speed and precision, making it the optimal choice for use in the ILFDS system. In this work, the YOLO-based detector is implemented as an application-oriented module within the ILFDS system for real-time droplet identification, rather than as an algorithmic contribution. The overall sorting performance is determined by the coordinated operation of multiple system components, including image quality during acquisition, flow stability in the microchannel, and the timing and strength of DEP actuation. Variations in any of these factors may affect the end-to-end detection and sorting accuracy.

Evaluation of networks for the detection of different targets

To evaluate the detection performance of the network for our ILFDS system, we use three types of samples (30 μm polystyrene particles, Haematococcus pluvialis, and Scenedesmus quadricauda) as targets encapsulated in droplets for network training and performance assessment. As illustrated in Fig. S6, the 30 μm polystyrene beads show a consistent size and opacity, while the Haematococcus pluvialis and Scenedesmus quadricauda show a significant morphological diversity within the 10–30 μm size range. We construct three datasets, each containing approximately 1000 images for each target type. Through network training on these datasets, we develop network models that are capable of accurately recognizing these three micro-targets.

To evaluate the classification performances for the three samples, we use the confusion matrix, P-R curve, and F1 score as the primary evaluation metrics. The performance parameters for the classification models include *Precision,* which is the proportion of correctly classified samples among those predicted to be of a certain category; *Recall,* which is the proportion of correctly classified samples among all actual samples of a certain category; and *Accuracy,* which is the proportion of correctly classified samples among all samples. Meanwhile, the *F1* score is a metric used in statistics to measure the accuracy of a binary classification model and represents the harmonic mean of precision and recall. The formulas for calculating these parameters are as follows[18,43]:

$$Precision = \frac{TP}{TP + FP} \tag{1}$$

$$Recall = \frac{TP}{TP + FN} \tag{2}$$

$$Accuracy = \frac{TP + TN}{TP + TN + FP + FN} \tag{3}$$

$$F1 = 2 \times \frac{Precision \times Recall}{Precision + Recall} \tag{4}$$

In these formulas, TP (True Positive) is the count of samples correctly predicted as positive. TN (True Negative) is the count of samples correctly predicted as negative. FP (False Positive) is the count of samples incorrectly predicted as positive, and FN (False Negative) is the count of samples incorrectly predicted as negative.

Specifically, the subplots (i) in Fig. 3a–c illustrate the classification differences of the three different samples during real-time detection. Subplots (ii) in Fig. 3a–c show the confusion matrices for the three samples. The detection accuracies of single-target droplets all exceed 96% for 30 μm particles, high-concentration *Haematococcus pluvialis*, and low-concentration *Scenedesmus quadricauda*. The impurities in microchannel backgrounds are a primary cause of FP. To improve the detection accuracy, the confidence threshold is set at 0.6 to capture more potential targets, while the IOU threshold is set at 0.65 to ensure a strong overlap between the predicted and actual targets. These parameters are chosen based on iterative experiments to ensure a robust balance between sensitivity and specificity. Therefore, the network is optimized using the FP metric in the confusion matrix to distinguish impurities from actual targets.

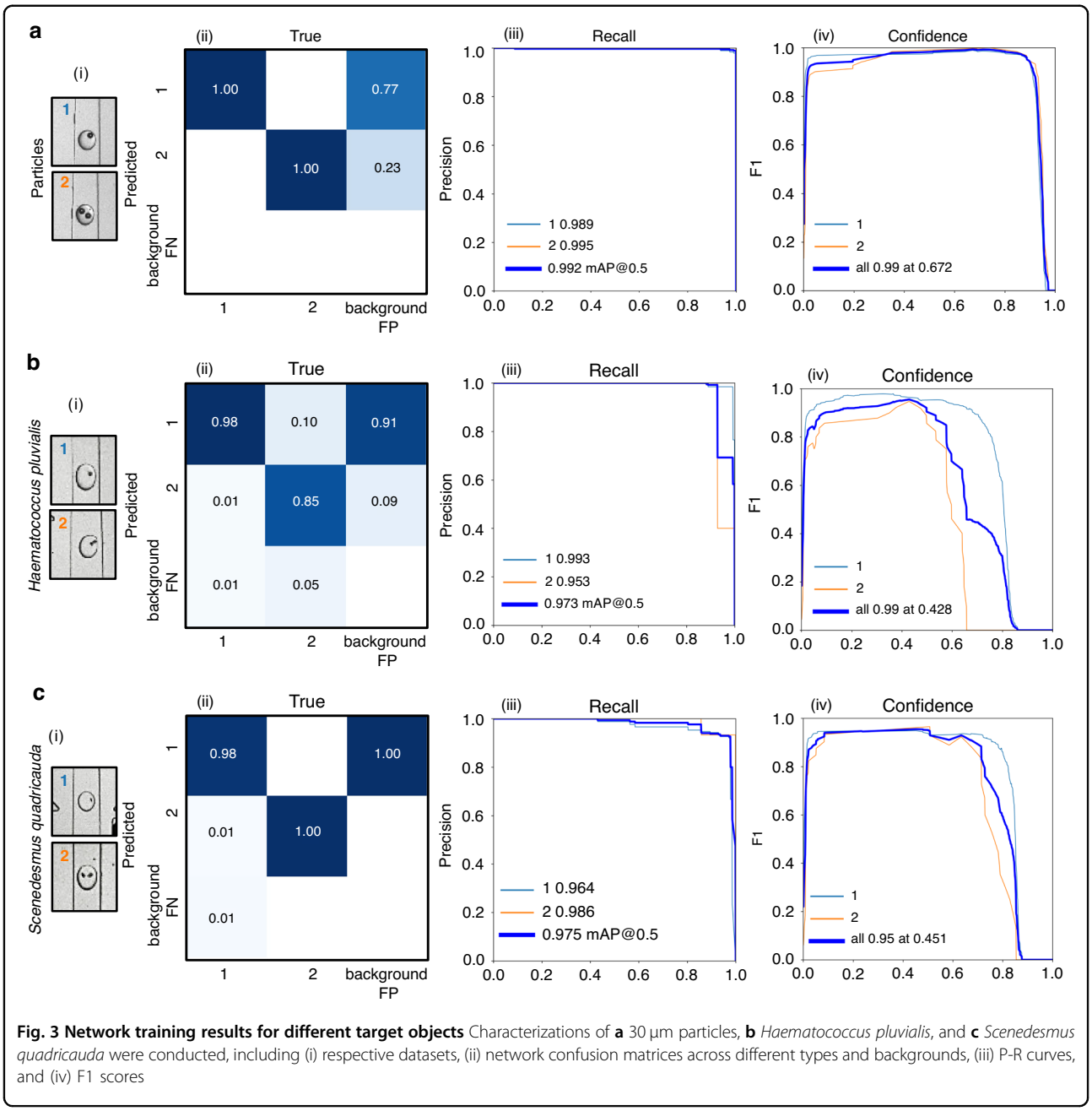

Fig. 3 Network training results for different target objects Characterizations of **a** 30 μm particles, **b** *Haematococcus pluvialis*, and **c** *Scenedesmus quadricauda* were conducted, including (i) respective datasets, (ii) network confusion matrices across different types and backgrounds, (iii) P-R curves, and (iv) F1 scores

As illustrated in the subplot (iii) of Fig. 3a–c, the P-R curve is used as a key indicator to evaluate performance on imbalanced datasets and real-time target detection capabilities[44]. The P-R curve demonstrates that the 30 μm particle model maintains robust performances across various decision thresholds, particularly in the high recall region. Our ILFDS system achieves a detection accuracy of 99.2% when using mAP@0.5 as the primary evaluation criterion. Although the accuracy for algae samples slightly decreases due to the morphological differences, the overall detection accuracies remain as high as 97.3% for *Haematococcus pluvialis* and 97.5% for *Scenedesmus quadricauda*. And subplot (iv) in Fig. 3a–c presents the F1 curves of the three detection models, the 30 μm particle model reaches an F1 score peak close to 1.0 at a confidence level of 0.7, indicating an optimal balance between precision and recall at this threshold. The *Haematococcus pluvialis* and *Scenedesmus quadricauda* models achieve their highest F1 scores at confidence levels of 0.46 and 0.67, respectively.

To further validate the accuracy of the trained models, the detection performance is tested using a validation set.

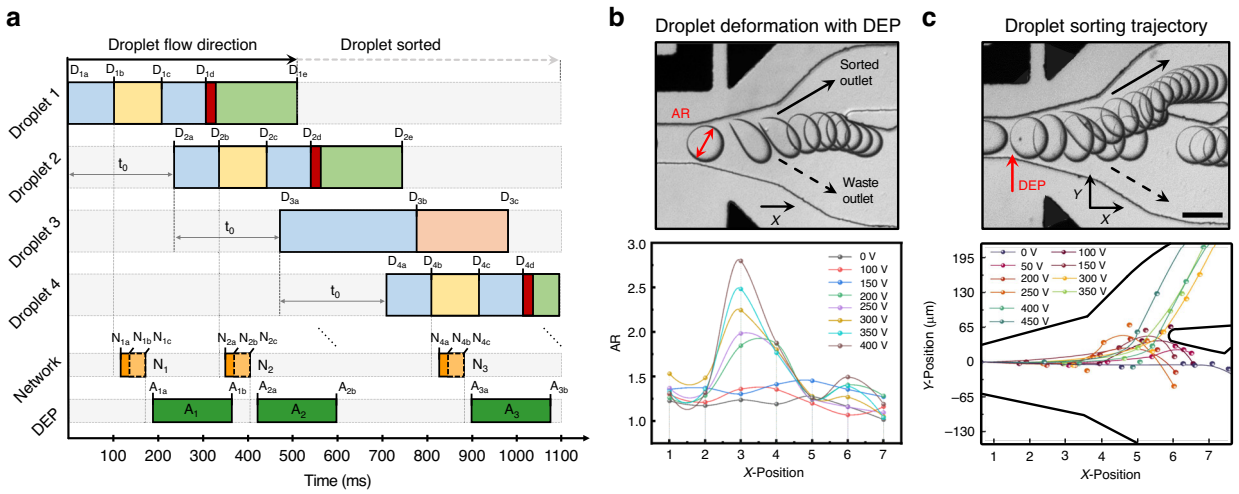

Fig. 4 Real-time detection and sorting procedures and droplet deformation analysis a Real-time detection, sorting, and signal processing procedures of target droplets (Droplets 1, 2, and 4) and non-target droplets (Droplet 3). **b** Deformation factors AR of droplets under different voltages. **c** Droplets sorting trajectories under different voltages. The scale bar is 100 μm

The image sequence in Fig. S7A clearly shows that each droplet containing target particles is accurately identified by the model. Based on these results, the detection threshold is set to be 0.65. Additionally, a comparative analysis of the mAP@0.5 precision during the training process of different network models is conducted using TensorBoard. As shown in Fig. S7B, all three models achieve over 90% precision by the 100th epoch, indicating that the models are well-trained and show a high detection performance. However, the different final performances among the models are influenced by the sample concentration. Among the three models, as depicted in Fig. S8, the detection accuracy for *Scenedesmus quadricauda* was the lowest.

Integration of YOLO-D detection with dielectrophoretic sorting in the ILFDS system

To achieve high-precision droplet sorting, our ILFDS system integrates YOLO-D detection with DEP sorting. The YOLO-D network accurately identifies target droplets in images and generates specific identification signals. These signals are then processed by a specially designed droplet sorting controller, which matches the signals to the corresponding droplets. The controller triggers DEP forces to sort the droplets in real-time. By controlling the DEP sorting based on the network's signals, the system ensures precise detection and sorting of target droplets. Furthermore, our ILFDS system reduces the false positives and maintains a high recall rate by only sorting droplets identified with a confidence level above the set threshold.

As depicted in Fig. 4a, each target droplet sequentially undergoes inflow, image detection, delay-based signal processing, DEP actuation, and final collection. After a target droplet enters the detection region, the trained network identifies its category and determines its distance to the sorting reference point. Based on the preset droplet velocity and the system delay associated with image acquisition, neural network processing, and signal transmission, the controller calculates the required triggering interval and applies the DEP actuation signal before the droplet reaches the sorting junction. To ensure reliable sorting, the DEP force must be activated early enough to laterally deflect the target droplet into the collection channel, while being terminated before the following droplet enters the actuation region to avoid cross-interference between adjacent droplets. In contrast, non-target droplets do not trigger the actuation signal and therefore continue along their default trajectories into the waste outlet. This timing coordination between detection, signal processing, and DEP actuation is critical for maintaining sorting accuracy and reliability under continuous-flow conditions.

Besides, the selection of DEP voltage plays an important role in the undamaged sorting of droplets in the ILFDS system. In Fig. 4b, an analysis is provided for understanding the deformation of droplets under the voltages of 0–400 V. The small deformation enables accurate routing of droplets into the target channel without compromising their integrity. The flow rates for the oil phase, aqueous phases, and spacing oil are set to be 260 μL/h, 10 μL/h, and 80 μL/h, respectively. To precisely measure this deformation, an aspect ratio (AR)[45] is defined:

$$\delta = \frac{a^2}{b^2} - 1 \tag{5}$$

where a represents the semi-major axis radius, and b represents the semi-minor axis radius. It is observed that at voltages below 150 V, significant fluctuations occur primarily between positions 4 and 6. As shown in Fig. 4b, droplet deformation becomes significant when the applied voltage exceeds 250 V. At voltages above 350 V, the AR surpasses 2.5, which could potentially compromise cell viability. Therefore, an optimal voltage range of 250 V to 350 V is selected to ensure effective sorting.

The trajectories of droplets at different voltages are shown in Fig. 4c. The DEP effects cause these trajectories to vary with voltages. As the sorting voltage increases, the paths of droplets gradually shift toward the sorted outlet. Notably, beyond 250 V, the droplet trajectories clearly demonstrate effective sorting. Experimental observations indicate that within the voltage range of 250–350 V, optimal droplet sorting is achieved in our ILFDS system. This voltage range ensures efficient sorting while maintaining droplet integrity.

Sorting of single-target encapsulated droplets using the ILFDS system

Precise single-target encapsulation is essential for applications such as single-cell sequencing and cell therapy, where downstream analysis relies on high-purity and well-isolated cellular inputs. However, conventional microfluidic encapsulation techniques typically rely on passive loading governed by Poisson distribution, resulting in a high proportion of empty or multi-target droplets. This randomness not only leads to significant sample waste but also complicates data interpretation. To overcome this challenge, our ILFDS system integrates high-precision image detection with real-time sorting, enabling active identification and sorting of single-target droplets with high efficiency and accuracy.

To demonstrate the performance of our ILFDS system for sorting single-target encapsulated droplets, real-time detection and sorting experiments are conducted using 30 μm particles (Fig. 5a), *Haematococcus pluvialis* (Fig. 5b), and *Scenedesmus quadricauda* (Fig. 5c). These experiments evaluate the system's efficiency with varying concentrations, morphologies, and quantities. Figure 5a shows the real-time observation of the target droplet sorting process. The target droplets containing a single 30 μm particle are marked with red arrows, while empty or multi-target droplets are indicated by black arrows. The detection region of the microfluidic chip is highlighted in blue, and the green area serves as a distance reference marker for the droplets. Each image is annotated with a number representing the running time of the ROS node corresponding to the current motion state of the droplets.

As shown in Fig. 5, our ILFDS system achieves high detection efficiencies: 99.2% ± 0.75% for 30 μm polystyrene particles, 98.75% ± 1.34% for *Haematococcus pluvialis*, and 98.89% ± 1.05% for *Scenedesmus quadricauda*. During sorting, optimizing the voltage to 290 V and adjusting the sorting controller to approximately 290 pulses enable the precise collection of single-target droplets. The sorting efficiencies are 99.7% ± 0.25% for 30 μm polystyrene particles, 97.67% ± 2.78% for *Haematococcus pluvialis*, and 91.59% ± 1.27% for *Scenedesmus quadricauda*, respectively. The working process for sorting 30 μm polystyrene particles is further displayed in the Supplementary Video 1. Data analysis also shows that the collection purities exceed 80% for all three targets, with 30 μm polystyrene particles achieving the highest purity of 95.18% ± 5.09%. These results highlight the high accuracy and high efficiency of our ILFDS system in droplet detection and sorting. The formulas for calculating system efficiencies are as follows:

$$Detection\ Efficiency = \frac{Detected\ target\ count}{Actual\ target\ count} \tag{6}$$

$$Sorting\ Efficiency = \frac{Sorted\ target\ count}{Actual\ target\ count} \tag{7}$$

$$Collection\ Purity = \frac{Sorted\ target\ count}{Actual\ sorted\ count} \tag{8}$$

Among these, the detected target count is the number of target droplets identified by the system. Actual target count is the number of target droplets that pass through the detection area. The sorted target count is the number of target droplets sorted by the system. The actual sorted count is the number of droplets sorted by the system.

In the study of single-target droplet sorting using our ILFDS system, statistical data reveal improvements in sample purity before and after sorting, demonstrating the system's effectiveness in overcoming the limitations of the Poisson distribution. For droplets containing a larger number of encapsulated targets, detection performance may be affected by overlap and reduced image distinguishability, indicating that the practical upper limit is governed by image-based separability rather than a strict system constraint.

As shown in Fig. 5, for 30 μm polystyrene particles, the proportion of single-target droplets increases from 30.20% before sorting to 95.18% after sorting, corresponding to an approximately 3.15-fold improvement. For *Haematococcus pluvialis*, the proportion of single-target droplets increases from 6.80% to 77.30%, corresponding to an approximately 11.37-fold improvement. For *Scenedesmus quadricauda*, the proportion of single-target droplets increases from 17.20% to 79.0%, corresponding to an approximately 4.59-fold improvement. Although DEP actuation is applied at the droplet level, the overall sorting performance remains target-dependent because the reported DE, SE, and CP reflect the

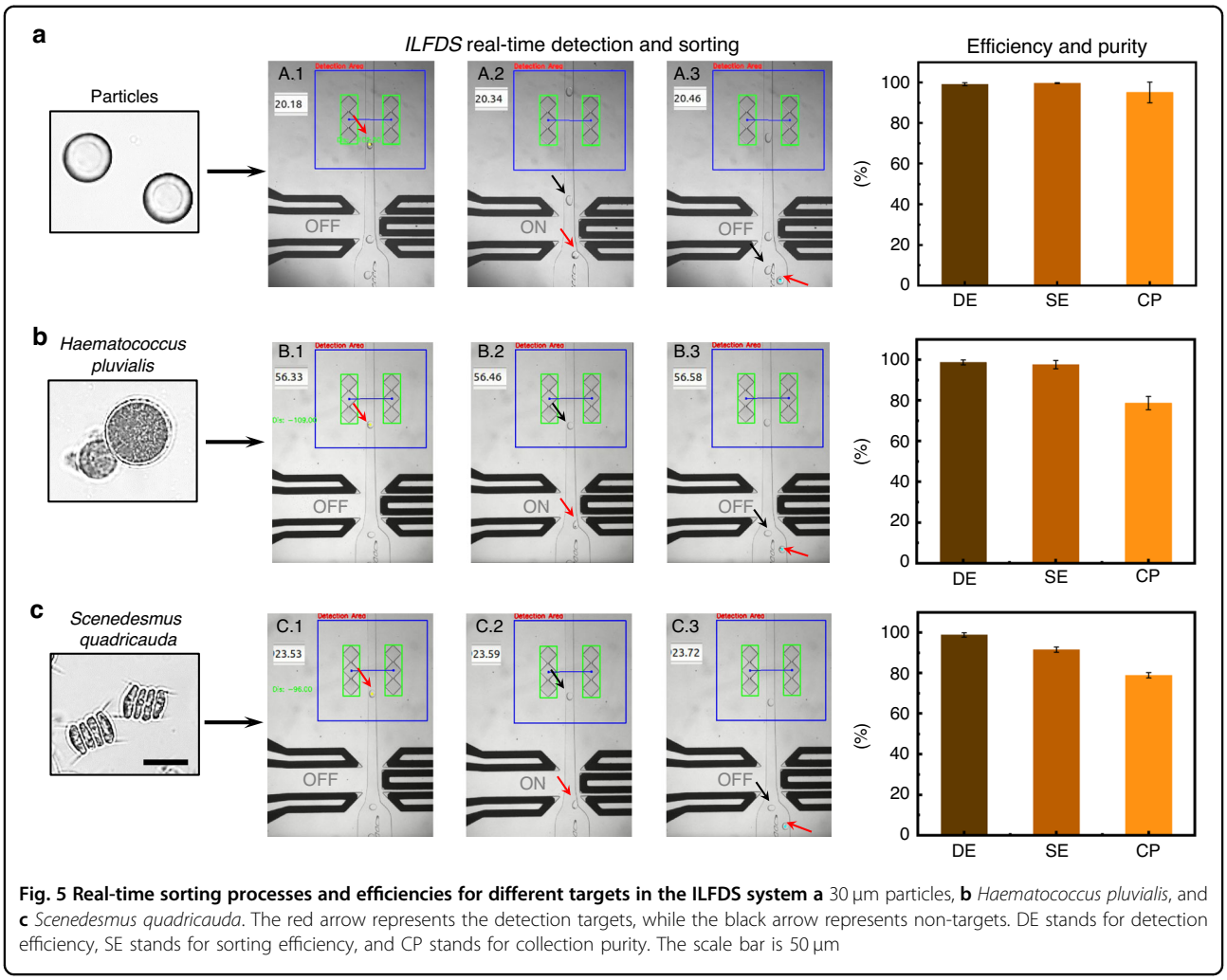

Fig. 5 Real-time sorting processes and efficiencies for different targets in the ILFDS system a 30 μm particles, **b** *Haematococcus pluvialis*, and **c** *Scenedesmus quadricauda*. The red arrow represents the detection targets, while the black arrow represents non-targets. DE stands for detection efficiency, SE stands for sorting efficiency, and CP stands for collection purity. The scale bar is 50 μm

combined effects of image recognition, timing control, and post-sorting collection. The 30 μm beads exhibit the highest performance due to their uniform size, shape, and optical appearance, whereas the algal samples show greater variability in morphology, orientation, and image contrast. In addition, differences in initial single-target occupancy also contribute to variations in collection purity. As a result, the end-to-end sorting metrics differ slightly among beads and the two cell types, despite sharing the same DEP deflection mechanism.

High-throughput morphology-based cell sorting using the ILFDS system

Beyond the sorting of single-target encapsulated droplets, the system has also demonstrated the capability to effectively sort mixed samples based on their morphological features. The sorting experiments of mixed algae solutions at a high flow rate are conducted. Specifically, we select a sample with mixed *Euglena gracilis* (elongated morphology) and *Haematococcus pluvialis* (spherical morphology) (Fig. S10) and conduct experiments to sort droplets encapsulated with the target algae. The water phase flow rate for droplet generation is set at 30 μL/h, the oil phase flow rate is set at 400 μL/h, and the spacing oil phase flow rate is set at 600 μL/h. As shown in Fig. 6a, b, the target droplets encapsulated with *Euglena gracilis* are identified in the preset detection area and subsequently deflected into the target channel under DEP actuation. A similar process is observed for *Haematococcus pluvialis*, as shown in Fig. 6c, d. As summarized in Fig. 6e, the DE, SE, and CP for *Euglena gracilis* were 90.47% ± 2.72%, 90.20% ± 1.04%, and 85.00% ± 2.65%, respectively, while those for *Haematococcus pluvialis* were 91.03% ± 3.35%, 89.03% ± 3.92%, and 79.53% ± 1.19%, respectively. The sorting processes of *Euglena gracilis* are displayed in the Supplementary Video 2, while the sorting processes of *Haematococcus pluvialis* are displayed in the Supplementary Video 3. These results demonstrate that the ILFDS system can reliably identify and sort target droplets at a throughput of approximately 100 droplets s^{-1}, which reflects the droplet flow rate rather than a one-to-one correspondence with image frames. The YOLO-based detection operates within the real-time image-processing capability of the system, while

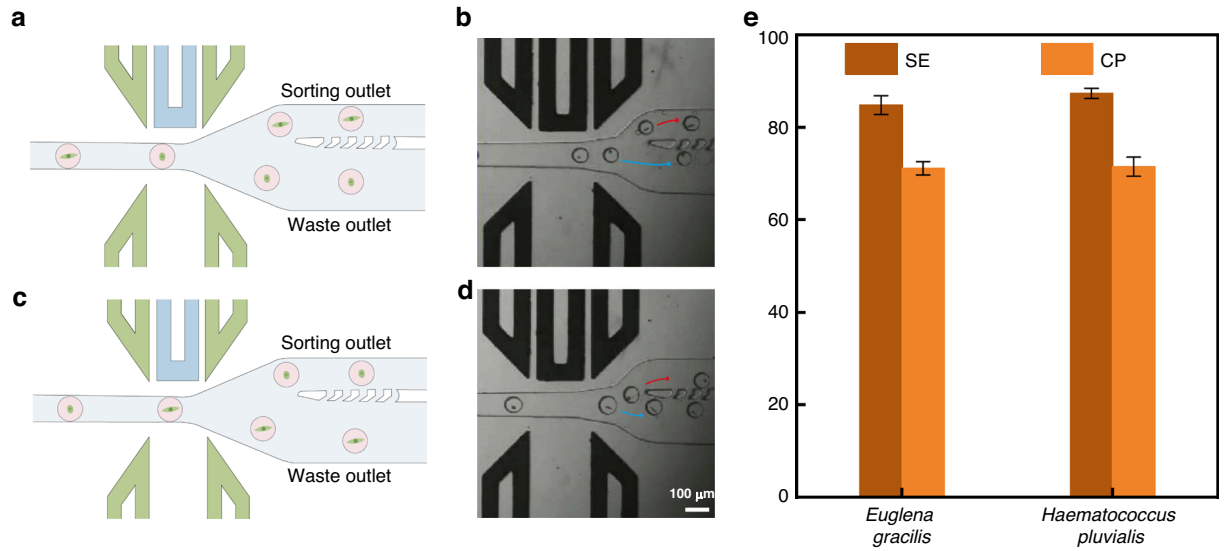

Fig. 6 Real-time detection and sorting of mixed algae solutions based on their morphological features using our ILFDS system. **a**, **b** Selective sorting of *Euglena gracilis* (elongated morphology) from a mixed algal population. **c**, **d** Selective sorting of *Haematococcus pluvialis* (spherical morphology) from the same mixture. **e** Quantitative evaluation of sorting efficiency (SE) and collection purity (CP) for both algal species. The scale bar is 100 μm

droplet spacing and delay-based actuation enable asynchronous detection and sorting, thereby supporting stable operation under continuous-flow conditions.

The performance of the ILFDS system is primarily constrained by the coupling between imaging speed, signal processing latency, and DEP actuation timing. In particular, the achievable throughput is limited by the balance between droplet generation frequency and the real-time processing capability of the detection and control pipeline. In addition, stable operation relies on consistent droplet spacing and flow conditions, as variations in droplet velocity or spacing may affect the synchronization accuracy between detection and actuation. Given these characteristics, the ILFDS system is particularly well-suited for applications requiring label-free, morphology-based sorting of micro-objects under continuous-flow conditions. Typical scenarios include single-cell analysis, microalgae screening, and other applications in which preserving cell viability and avoiding labeling steps are important. The combination of real-time image-based identification and on-demand DEP actuation provides a flexible platform for handling heterogeneous samples with varying sizes and morphologies.

Conclusion

In this study, we developed an ILFDS system that integrates droplet microfluidics, YOLO-D-based image recognition, and DEP sorting using liquid-metal electrodes. This system operates at low voltages (250–350 V) and achieves real-time sorting while maintaining droplet integrity and minimizing droplet deformation. Through comprehensive experiments, the ILFDS system demonstrates detection accuracies exceeding 98% and sorting efficiencies greater than 85% for 30 μm polystyrene particles, *Haematococcus pluvialis*, and *Scenedesmus quadricauda*. Notably, the proportion of single-target droplets increased by approximately 3.15-fold, 11.37-fold, and 4.59-fold for 30 μm polystyrene particles, *Haematococcus pluvialis*, and *Scenedesmus quadricauda*, respectively. Additionally, the ILFDS system successfully sorts mixed target solutions, achieving >90% detection efficiency and >89% sorting efficiency for mixed *Haematococcus pluvialis* and *Euglena gracilis* samples. These results validate the robustness of the ILFDS system in handling heterogeneous samples with high precision, demonstrating its potential to address limitations associated with conventional droplet encapsulation and detection strategies.

Acknowledgements
This research work is supported by the National Key Research and Development Program of China (2021YFC2103300), the National Natural Science Foundation of China (51875103 and 81727801), the Natural Science Foundation of Jiangsu Province (BK20190064), the '333' Project of Jiangsu Province, and the Basic Research Program of Jiangsu Province (BK20250646).

Author details
[1]School of Mechanical Engineering, and Jiangsu Key Laboratory for Design and Manufacture of Micro-Nano Biomedical Instruments, Southeast University, Nanjing, China. [2]Department of Mechanical Engineering, The University of Hong Kong, Pokfulam, Hong Kong, China. [3]Key Laboratory for Engineering Biology for Low-carbon Manufacturing, Tianjin Institute of Industrial Biotechnology, Chinese Academy of Sciences, Tianjin, China. [4]National Center of Technology Innovation for Synthetic Biology, Tianjin, China

Author contributions

Kefan Guo: Conceptualization, Experiment, Methodology, Data analysis, Writing - original draft. Qingqing Liu: Experiment, Data analysis, Writing - original draft. Huiling Yuan: Methodology, Investigation. Yuanyuan Zhang: Methodology, Investigation. Zhixian Zhu: Methodology, Investigation. Shu Zhu: Methodology, Investigation. Lin Jiang: Investigation. Qinhong Wang: Conceptualization, Methodology, Writing - review & editing, Funding acquisition, Supervision. Nan Xiang: Conceptualization, Methodology, Writing - review & editing, Funding acquisition, Supervision.

Data availability

All relevant data are within the manuscript and its additional files.

Conflict of interest

The authors declare no competing interests.

Supplementary information The online version contains supplementary material available at https://doi.org/10.1038/s41378-026-01349-3.

Received: 27 January 2026 Revised: 27 March 2026 Accepted: 13 April 2026
Published online: 05 June 2026

References

1. Stuart, T., Srivastava, A., Madad, S., Lareau, C. A. & Satija, R. Single-cell chromatin state analysis with Signac. *Nat. Methods* **18**, 1333–1341 (2021).
2. Lan, F., Demaree, B., Ahmed, N. & Abate, A. R. Single-cell genome sequencing at ultra-high-throughput with microfluidic droplet barcoding. *Nat. Biotechnol.* **35**, 640–646 (2017).
3. Sun, W. et al. snRNA-seq reveals a subpopulation of adipocytes that regulates thermogenesis. *Nature* **587**, 98–102 (2020).
4. Xu, Y., Wang, Z., Li, C., Tian, S. & Du, W. Droplet microfluidics: unveiling the hidden complexity of the human microbiome. *Lab Chip* **25**, 1128–1148 (2025).
5. Nan, L., Zhang, H., Weitz, D. A. & Shum, H. C. Development and future of droplet microfluidics. *Lab Chip* **24**, 1135–1153 (2024).
6. Kalucka, J. et al. Single-cell transcriptome atlas of murine endothelial cells. *Cell* **180**, 764–779.e720 (2020).
7. Stuart, T. & Satija, R. Integrative single-cell analysis. *Nat. Rev. Genet.* **20**, 257–272 (2019).
8. Zhu, S. et al. Microfluidic impedance cytometry for single-cell sensing: review on electrode configurations. *Talanta* **233**, 122571 (2021).
9. De Jonghe, J. et al. spinDrop: a droplet microfluidic platform to maximise single-cell sequencing information content. *Nat. Commun.* **14**, 4788 (2023).
10. Cao, J. et al. The single-cell transcriptional landscape of mammalian organogenesis. *Nature* **566**, 496–502 (2019).
11. Nawaz, A. A. et al. Intelligent image-based deformation-assisted cell sorting with molecular specificity. *Nat. Methods* **17**, 595–599 (2020).
12. Zeng, Y. et al. Miniaturizing chemistry and biology using droplets in open systems. *Nat. Rev. Chem.* **7**, 439–455 (2023).
13. Zhu, Z. et al. Free-boundary microfluidic platform for advanced materials manufacturing and applications. *Adv. Mater.* **36**, e2304840 (2023).
14. Xiang, N. & Ni, Z. Microfluidics for biomedical applications. *Biosensors* **13**, 161 (2023).
15. Zhong, J., Liang, M. & Ai, Y. DUPLETS: deformability-assisted dual-particle encapsulation via electrically activated sorting. *Small Methods* **7**, e2300089 (2023).
16. Zhu, S., Fang, Y., Guo, K., Ni, Z. & Xiang, N. Next-generation liquid biopsy instruments: challenges and opportunities. *Electrophoresis* **44**, 775–783 (2023).
17. Mc Veigh, M. & Bellan, L. M. Microfluidic synthesis of radiotracers: recent developments and commercialization prospects. *Lab Chip* **24**, 1226–1243 (2024).
18. Wang, B. et al. Smartphone-based platforms implementing microfluidic detection with image-based artificial intelligence. *Nat. Commun.* **14**, 1341 (2023).
19. Li, X., Zhao, D., Wang, Y. & Huang, H. Droplet-based cell-laden microgels for high-throughput analysis. *Trends Biotechnol.* **7799**, 00301–00303 (2023).
20. Jiang, J., Yang, G. & Ma, F. Fluorescence coupling strategies in fluorescence-activated droplet sorting (FADS) for ultrahigh-throughput screening of enzymes, metabolites, and antibodies. *Biotechnol. Adv.* **9**, 108173 (2023).
21. Nitta, N. et al. Intelligent image-activated cell sorting. *Cell* **175**, 266–276.e213 (2018).
22. Baret, J. C. et al. Fluorescence-activated droplet sorting (FADS): efficient microfluidic cell sorting based on enzymatic activity. *Lab Chip* **9**, 1850–1858 (2009).
23. Ott, F., Meyer-Zedler, T., Schmitt, M. & Popp, J. Image-based fuzzy logic control for pressure-driven droplet microfluidics as autosampler for multimodal imaging microscopy. *Lab Chip* **25**, 119–126 (2025).
24. Siu, D. M. D. et al. Optofluidic imaging meets deep learning: from merging to emerging. *Lab Chip* **23**, 1011–1033 (2023).
25. Li, P. et al. Detachable acoustophoretic system for fluorescence-activated sorting at the single-droplet level. *Anal. Chem.* **91**, 9970–9977 (2019).
26. LaBelle, C. A., Massaro, A., Cortes-Llanos, B., Sims, C. E. & Allbritton, N. L. Image-based live cell sorting. *Trends Biotechnol.* **39**, 613–623 (2021).
27. Zhang, S., Li, H., Wang, K. & Qiu, T. Accelerating intelligent microfluidic image processing with transfer deep learning: a microchannel droplet/bubble breakup case study. *Sep. Purif. Technol.* **6**, 123703 (2023).
28. Hayashi, M. et al. Is AI essential? Examining the need for deep learning in image-activated sorting of Saccharomyces cerevisiae. *Lab Chip* **23**, 4232–4244 (2023).
29. Gu, Y. et al. Machine learning based real-time image-guided cell sorting and classification. *Cytom. Part A* **95a**, 499–509 (2019).
30. Sesen, M. & Whyte, G. Image-based single cell sorting automation in droplet microfluidics. *Sci. Rep.* **10**, 8736 (2020).
31. Howell, L., Anagnostidis, V. & Gielen, F. Multi-object detector YOLOv4-tiny enables high-throughput combinatorial and spatially-resolved sorting of cells in microdroplets. *Adv. Mater. Technol.* **7**, 2101053 (2021).
32. Yu, Z. et al. Droplet-based microfluidic screening and sorting of microalgal populations for strain engineering applications. *Algal Res.* https://doi.org/10.1016/j.algal.2021.102293 (2021).
33. Huang, C., Jiang, Y., Li, Y. & Zhang, H. Droplet detection and sorting system in microfluidics: a review. *Micromachines* https://doi.org/10.3390/mi14010103 (2022).
34. Schutz, S. S., Beneyton, T., Baret, J. C. & Schneider, T. M. Rational design of a high-throughput droplet sorter. *Lab Chip* **19**, 2220–2232 (2019).
35. Jiang, L., Liu, Q., Yang, H., Wang, Q. & Xiang, N. A low-voltage-driven droplet sorter for high-stability and small-deformation droplet sorting. *Electrophoresis* **46**, 1525–1533 (2025).
36. Anagnostidis, V. et al. Deep learning guided image-based droplet sorting for on-demand selection and analysis of single cells and 3D cell cultures. *Lab Chip* **20**, 889–900 (2020).
37. Liu, Z. et al. Gray-level guided image-activated droplet sorter for label-free, high-accuracy screening of single-cell on demand. *Small* **21**, e2500520 (2025).
38. Liu, Q. et al. An intelligent droplet sorter using optimized liquid-metal electrodes for droplet sorting under a low voltage. *Sens. Actuators B Chem.* https://doi.org/10.1016/j.snb.2024.136408 (2024).
39. Wang, Y., Wang, X., Pan, T., Li, B. & Chu, J. Label-free single-cell isolation enabled by microfluidic impact printing and real-time cellular recognition. *Lab Chip* **21**, 3695–3706 (2021).
40. Svensson, C. M. et al. Coding of experimental conditions in microfluidic droplet assays using colored beads and machine learning supported image analysis. *Small* **15**, e1802384 (2019).
41. Gardner, K. et al. Deep learning detector for high precision monitoring of cell encapsulation statistics in microfluidic droplets. *Lab Chip* **22**, 4067–4080 (2022).
42. Wang, J. et al. Predicting the fluid behavior of random microfluidic mixers using convolutional neural networks. *Lab Chip* **21**, 296–309 (2021).
43. Dong, H. et al. AI-enhanced biomedical micro/nanorobots in microfluidics. *Lab Chip* **1**, 1419–1440 (2024).
44. Zhong, J., Liang, M., Tang, Q. & Ai, Y. Selectable encapsulated cell quantity in droplets via label-free electrical screening and impedance-activated sorting. *Mater. Today Bio* **19**, 100594 (2023).
45. Shang, L., Cheng, Y. & Zhao, Y. Emerging droplet microfluidics. *Chem. Rev.* **117**, 7964–8040 (2017).